

Using coherent feedback for a periodic clock

Stefan Zeppetzauer ^{1,*} Leonardo Assis Morais ^{1,2} Xin He ¹ Gerard Milburn,¹ and Arkady Fedorov¹

¹*ARC Centre of Excellence for Engineered Quantum Systems,
School of Mathematics and Physics, The University of Queensland, St Lucia, Australia.*

²*Instituto Federal Fluminense, Campus Bom Jesus do Itabapoana,
Bom Jesus do Itabapoana, Rio de Janeiro, Brazil*

(Dated: October 31, 2024)

A driven linear oscillator and a feedback mechanism are two necessary elements of any classical periodic clock. Here, we introduce a novel, fully quantum clock using a driven oscillator in the quantum regime and coherent quantum feedback. We show that if we treat the model semiclassically, this system supports limit cycles, or self-sustained oscillations, as needed for a periodic clock. We then analyse the noise of the system quantum mechanically and prove that the accuracy of this clock is higher compared to the clock implemented with the classical measurement feedback. We experimentally implement the model using two superconducting cavities with incorporated Josephson junctions and microwave circulators for the realisation of the quantum feedback. We confirm the appearance of the limit cycle and study the clock accuracy both in frequency and time domains. Under specific conditions of noisy driving, we observe that the clock oscillations are more coherent than the drive, pointing towards the implementation of a quantum autonomous clock.

I. INTRODUCTION

A clock is a driven, stable oscillator (limit cycle) with a counter [1]. Clocks make use of feedback to regulate the period of the oscillation [2] (see Appendix A for more details on the role of limit cycles in clock design). In classical physics, all feedback is equivalent to measurement-based feedback. In a quantum clock oscillator, feedback based on continuous measurement necessarily adds noise as the measurement currents carry quantum measurement noise and this drives noise in the clock oscillator. However, there is a distinctly quantum form of feedback, called coherent feedback, that makes use of circulators to break time-reversal invariance. This form of feedback does not use measurement currents but rather uses unidirectional propagating quantum fields directly [3, 4]. A quantum clock built using coherent feedback must necessarily be less noisy than a clock that uses measurement feedback control.

Here, we propose and demonstrate a novel quantum clock using coherent feedback in a superconducting circuit. Since the feedback does not involve readout, there is no quantum measurement noise imposed on the feedback signal, allowing us to investigate and characterise the inherent quantum noise of the system and its effects on the clock properties. Our quantum clock is composed of two high-Q cavities coupled by coherent feedback [3]. A semiclassical analysis shows that limit cycles are possible and can therefore be used to implement stable clock oscillations. This analysis does not take into account noise. In order to find the precision of the clock, both quantum and classical noise need to be included. At low temperature, the quantum noise dominates, and in this limit,

the precision of the clock can be bounded by the recently developed thermodynamic uncertainty relations [5].

This paper is structured as follows. Section II presents the proposed model for a quantum clock using coherent feedback and derives the master equation that describes its dynamics using the SLH framework. The semiclassical equations of motion are derived from the master equation, and the limits where this approximation holds are discussed. A linear stability analysis of the fixed points is performed, showing that a supercritical Hopf bifurcation appears in the system. The master equation for a measurement-based feedback clock is also derived to demonstrate the equivalency to the coherent feedback clock. Section III compares how noise affects both measurement-based and coherent feedback clocks, theoretically demonstrating the advantage of coherent feedback for clock accuracy. Section IV details the experimental realisation of the model using superconducting microwave resonators and Josephson junctions. The results of the measurements are presented in Section V, demonstrating the emergence of limit cycles and studying their properties and the resulting clock accuracy as a function of external parameters. The results are summarised, and the outlook is presented in Section VI.

II. MODEL

Our clock scheme is shown in Fig. 1. It consists of a superconducting microwave circuit composed of two coplanar waveguide resonators: a quarter-wavelength resonator (A) and a half-wavelength (B). They are connected by microwave transmission lines via coupling capacitors. Resonator B is coherently driven by an external electromagnetic field of amplitude ϵ and frequency ω_ϵ . With respect to the driving field, both resonators are

* To whom correspondence should be addressed:
s.zeppetzauer@uq.edu.au

detuned by

$$\Delta_i = \omega_i - \omega_\epsilon, \quad (1)$$

where ω_i is the resonance frequency for resonator i , with $i = a, b$. Both resonators incorporate Josephson junctions providing a Kerr-type nonlinearity of strength K_i . The total decay rates of the resonators, κ_i , consist of the coupling rates for each side of the resonators and the internal losses.

To study the dynamics of our clock system, we use the master equation under Born-Markov approximations [6]:

$$\dot{\rho} = -\frac{i}{\hbar}[\hat{H}, \rho] + \sum_i \mathcal{D}[\hat{L}_i]\rho, \quad (2)$$

where ρ is the composite quantum state that describes the intracavity field for both resonators, H is the system Hamiltonian, and L_i are the collapse operators. The superoperator \mathcal{D} is defined as

$$\mathcal{D}[\hat{L}_i]\rho = \hat{L}_i^\dagger \rho \hat{L}_i - \frac{1}{2}(\hat{L}_i^\dagger \hat{L}_i \rho + \rho \hat{L}_i^\dagger \hat{L}_i). \quad (3)$$

To obtain the Hamiltonian \hat{H} and the jump operators \hat{L}_i for our coherent clock, we use the SLH framework [7, 8], which provides a set of algebraical rules to model complex quantum networks from basic components. Details about the decomposition of our system in terms of SLH components are discussed in Appendix B. The resulting Hamiltonian that describes our model

is given by (note that $\hbar = 1$)

$$\begin{aligned} \hat{H} = & K_a \hat{a}^{\dagger 2} \hat{a}^2 + \Delta_a \hat{a}^\dagger \hat{a} + K_b \hat{b}^{\dagger 2} \hat{b}^2 + \Delta'_b \hat{b}^\dagger \hat{b} \\ & + \frac{i}{2} \sqrt{\kappa_{a_1}} \left[\sqrt{\kappa_{b_1}} (1 - \eta_1^2) e^{-i\phi_1} - \sqrt{\kappa_{b_2}} (1 - \eta_2^2) e^{i\phi_2} \right] \hat{a}^\dagger \hat{b} \\ & - i \sqrt{\kappa_{b_1}} \epsilon \hat{b}^\dagger + c.c., \end{aligned} \quad (4)$$

with

$$\Delta'_b = \Delta_b + \sqrt{\kappa_{b_1} \kappa_{b_2}} \sqrt{(1 - \eta_1^2)(1 - \eta_2^2)} \sin(\phi_1 + \phi_2), \quad (5)$$

where $\hat{i}(\hat{i}^\dagger)$ is the creation (annihilation) operator, $K_{a,b}$ are the Kerr nonlinearity coefficients, κ_{a_1, b_1, b_2} are the coupling rates of the resonator ports and ϵ is the amplitude of the driving field. While the loss mechanisms from elements between the resonators such as the circulators are typically small at operating temperatures, they still influence the parameter regime where limit cycles occur and should not be neglected. We account for losses in the circulators by the insertion loss parameter $0 \leq \eta_i \leq 1$ with $i = 1, 2$. It is defined as the amplitude ratio of the lost (absorbed or reflected) to incident signal in the forward direction. The phases, ϕ_i , are the acquired phases for the electromagnetic field while it travels between cavities, and ϵ is the amplitude of the driving field. The quadratic terms describe the Kerr-type nonlinearity introduced in each cavity by the Josephson junction. Note that resonator B can be, in principle, fully linear. Our reason for introducing a tunable nonlinearity, in form of a superconducting quantum interference device (SQUID), is to be able to modulate the detuning to reach the necessary conditions for the emergence of a limit cycle. The collapse operators for the superconducting clock are

$$\hat{\mathbf{L}} = \begin{pmatrix} -\eta_1 \sqrt{\kappa_{a_1}} e^{i\phi_1} \hat{a} - \eta_1 \sqrt{\kappa_{b_2}} \sqrt{1 - \eta_2^2} e^{i(\phi_1 + \phi_2)} \hat{b} \\ \sqrt{\kappa_{a_{\text{int}}}} \hat{a} \\ \sqrt{\kappa_{a_1}} \sqrt{1 - \eta_1^2} e^{i\phi_1} \hat{a} + \left(\sqrt{\kappa_{b_1}} + \sqrt{\kappa_{b_2}} \sqrt{(1 - \eta_1^2)(1 - \eta_2^2)} e^{i(\phi_1 + \phi_2)} \right) \hat{b} \\ -\eta_2 \sqrt{\kappa_{b_2}} e^{i\phi_2} \hat{b} \\ \sqrt{\kappa_{b_{\text{int}}}} \hat{b} \end{pmatrix}, \quad (6)$$

where the first entry describes the feedback between the cavities and the first and third entry account for the internal losses of the resonators given by the rates $\kappa_{i_{\text{int}}}$ with $i = a, b$. It is worth noting that we neglect additional loss mechanism and imperfections such as reflections and circulator isolation, which should be taken into account if a more precise prediction is required. Since we are only interested to find an approximate parameter regime, we do not include these factors here.

A. Obtaining semiclassical equations

Using the Hamiltonian and collapse operators, we can calculate the master equation from which the expectation values for the annihilation operators for both cavities can be obtained by

$$\frac{d}{dt} \langle \hat{a} \rangle = \text{Tr}[\hat{a} \dot{\rho}], \quad \frac{d}{dt} \langle \hat{b} \rangle = \text{Tr}[\hat{b} \dot{\rho}]. \quad (7)$$

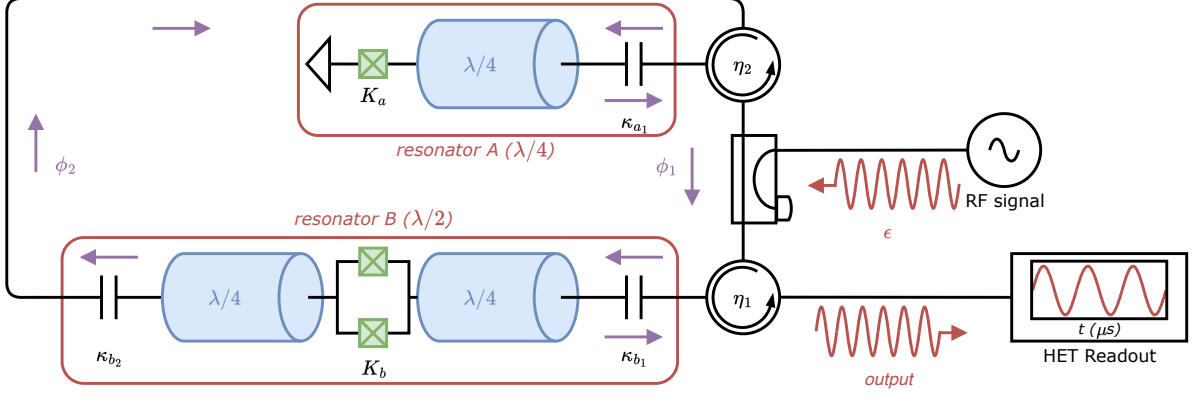


FIG. 1: Coherent feedback clock schematic: The incoming drive is injected into the circuit by a directional coupler. The clock resonator of length $\lambda/2$ is coupled to a transmission line on both ends via capacitors with coupling rates κ_{b_1} and κ_{b_2} . A SQUID is embedded in the centre of the resonator, consisting of a loop of Josephson junctions, depicted as a green box with a cross to tune its frequency by an external flux threaded through the SQUID loop. Microwaves reflected from the input port are fed into the readout chain for heterodyne (HET) readout by the first circulator. Signal leaking through another end is directed to the feedback resonator by the second circulator. The feedback resonator of length $\lambda/4$ is shorted to ground via a Josephson junction which generates the Kerr nonlinearity K_a on one end and capacitively coupled to a transmission line with rate κ_{a_1} . Incoming signals are reflected and eventually fed back to the clock resonator.

From this, we get:

$$\begin{aligned} \frac{d}{dt} \langle \hat{a} \rangle = & - \left(i\Delta_a + \frac{\kappa_a}{2} \right) \langle \hat{a} \rangle - 2iK_a \langle \hat{a}^\dagger \hat{a}^2 \rangle \\ & - \sqrt{1 - \eta_2^2} e^{i\phi_2} \sqrt{\kappa_{a_1} \kappa_{b_2}} \langle \hat{b} \rangle, \end{aligned} \quad (8)$$

$$\begin{aligned} \frac{d}{dt} \langle \hat{b} \rangle = & - \left(i\Delta'_b + \frac{\kappa_b}{2} \right) \langle \hat{b} \rangle - \sqrt{1 - \eta_1^2} e^{i\phi_1} \sqrt{\kappa_{a_1} \kappa_{b_1}} \langle \hat{a} \rangle \\ & - \sqrt{1 - \eta_1^2} \sqrt{\kappa_{b_1}} \bar{\epsilon}, \end{aligned} \quad (9)$$

where we define the total loss rates

$$\kappa_a = \kappa_{a_1} + \kappa_{a_{\text{int}}} \quad (10)$$

and

$$\begin{aligned} \kappa_b = & \kappa_{b_1} + \kappa_{b_2} + \kappa_{b_{\text{int}}} \\ & + 2\sqrt{\kappa_{b_1} \kappa_{b_2}} \sqrt{(1 - \eta_1^2)(1 - \eta_2^2)} \cos(\phi_1 + \phi_2). \end{aligned} \quad (11)$$

The semiclassical approximation is obtained by associating α and β , the classical complex amplitudes of the intracavity electromagnetic field, with the average values $\langle a \rangle$ and $\langle b \rangle$ obtained from the master equation, respectively. Additionally, we assume that the intracavity states remain approximately coherent, i.e.,

$$\langle a^\dagger a^2 \rangle \approx \alpha |\alpha|^2. \quad (12)$$

The semiclassical equations of motion for our coherent feedback clock are:

$$\dot{\alpha} = - \left(i\Delta_a + \frac{\kappa_a}{2} \right) \alpha - 2iK_a |\alpha|^2 \alpha - g_a e^{i\phi_2} \beta \quad (13)$$

$$\dot{\beta} = - \left(i\Delta'_b + \frac{\kappa_b}{2} \right) \beta - 2iK_b |\beta|^2 \beta - g_b e^{i\phi_1} \alpha - \bar{\epsilon}, \quad (14)$$

where $g_a = \sqrt{1 - \eta_2^2} \sqrt{\kappa_{a_1} \kappa_{b_2}}$ and $g_b = \sqrt{1 - \eta_1^2} \sqrt{\kappa_{a_1} \kappa_{b_1}}$ are coupling constants arising from coherent feedback. The effective driving field of cavity B is $\bar{\epsilon} = \sqrt{1 - \eta_1^2} \sqrt{\kappa_{b_1}} \epsilon$.

Since these two equations have complex solutions, we define

$$\alpha(t) := x_a(t) + iy_a(t), \quad \beta(t) := x_b(t) + iy_b(t). \quad (15)$$

The dynamics of the dynamical system can then be analysed using four equations in terms of the field quadratures x_j, y_j , with $j = a, b$ as follows

$$\begin{aligned} \dot{x}_a = & 2K_a y_a^3 + 2K_a x_a^2 y_a + \Delta_a y_a - \frac{\kappa_a}{2} x_a \\ & - g_a (\cos(\phi_2) x_b - \sin(\phi_2) y_b), \end{aligned} \quad (16)$$

$$\begin{aligned} \dot{y}_a = & -2K_a x_a^3 - 2K_a y_a^2 x_a - \Delta_a x_a - \frac{\kappa_a}{2} y_a \\ & - g_a (\sin(\phi_2) x_b + \cos(\phi_2) y_b), \end{aligned} \quad (17)$$

$$\begin{aligned} \dot{x}_b = & 2K_b y_b^3 + 2K_b x_b^2 y_b + \Delta'_b y_b - \frac{\kappa_b}{2} x_b \\ & - g_b (\cos(\phi_1) x_a - \sin(\phi_1) y_a) - \bar{\epsilon}, \end{aligned} \quad (18)$$

$$\begin{aligned} \dot{y}_b = & -2K_b x_b^3 - 2K_b y_b^2 x_b - \Delta'_b x_b - \frac{\kappa_b}{2} y_b \\ & - g_b (\sin(\phi) x_a + \cos(\phi) y_a), \end{aligned} \quad (19)$$

where we assume $\epsilon \in \mathcal{R}$ without loss of generality.

The effect of the feedback is similar to parametric amplification as x_a is coupled to x_b and y_a is coupled to y_b . In the case that $\kappa_{b_1} = \kappa_{b_2} = \kappa_b$ the effective gain rates for each quadrature is $\sqrt{\kappa_{a_1} \kappa_b}$. This would lead to an instability once this exceeds the loss rate for each cavity. However, the Kerr nonlinearity prevents this from occurring, leading to an effective gain saturation.

B. Fixed points and stability analysis

Our final goal is to find a set of physical parameters that allow us to use the model proposed here as a clock. To do so, we need to evaluate the dynamics of the vector fields described by Eqs. (16-19), analysing how their dynamics depends on the physical parameters. The first step is to find the fixed points $x_a^*, y_a^*, x_b^*, y_b^*$ for different values of the driving field ϵ . We solve the equations,

$$\dot{x}_a = 0, \dot{x}_b = 0, \dot{y}_a = 0, \dot{y}_b = 0, \quad (20)$$

using the Mathematica solver NSolve. Since our problem is four dimensional, we plot the intensities of the intracavity fields,

$$|\alpha|^2 = x_a^2 + y_a^2, \quad |\beta|^2 = x_b^2 + y_b^2, \quad (21)$$

as a function of the intensity of the driving field, $|\epsilon|^2$. The results are shown in Fig. 2.

The occurrence of limit cycles is often related to changes in the stability of fixed points. Therefore, to investigate under which conditions the limit cycles occur, we analyse the stability of the fixed points through a linear stability analysis of each fixed point. By calculating the Jacobian \mathcal{J} at a fixed point \mathbf{x}^* , we can determine the behaviour of the vector field in the vicinity of \mathbf{x}^* . In our case, the \mathcal{J} is a 4×4 matrix with each element given by

$$\mathcal{J}_{ij} = \frac{df_i}{dz_j}, \quad (22)$$

where f_i are the vector fields $\dot{x}_a, \dot{x}_b, \dot{y}_a, \dot{y}_b$ and z_j is one of the four real variables x_a, y_a, x_b, y_b . Once \mathcal{J} is found and evaluated at a given fixed point \mathbf{x}^* , we can find its eigenvalues and eigenvectors. From the eigenvalues λ_i , we can determine the stability of the fixed point:

- When all $\text{Re}(\lambda_i) > 0$, the fixed point is classified as a repeller or source: all nearby trajectories will exponentially diverge from the fixed point. Small perturbations will take the system away from the fixed point and the equilibrium is unstable.
- When all $\text{Re}(\lambda_i) < 0$, the fixed point is classified as an attractor or drain: all nearby trajectories will exponentially converge to the fixed point. After a small perturbation, the system will go back to the fixed point and the equilibrium is stable.

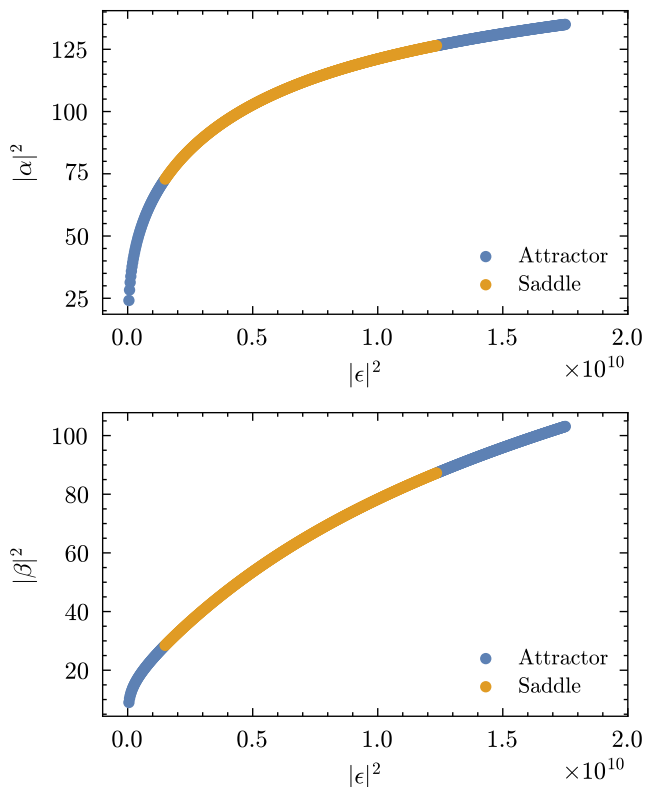


FIG. 2: Fixed points for the intensity of the intracavity field on resonators A and B, $|\alpha|^2$ and $|\beta|^2$, respectively, as a function of the intensity of the driving field $|\epsilon|^2$ in the semiclassical approximation. The parameters used in this simulation are: $\kappa_{b_1}/2\pi = \kappa_{b_2}/2\pi = 2.52 \times 10^6$, $\kappa_{b_{\text{int}}}/2\pi = 1.64 \times 10^6$, $\kappa_{a_1}/2\pi = 3.21 \times 10^6$, $\kappa_{a_{\text{int}}}/2\pi = 0.11 \times 10^6$, $\Delta_a/2\pi = \Delta_b/2\pi = 1.8 \times 10^6$, $\eta_1 = \sqrt{0.18}$, $\eta_2 = \sqrt{0.03}$, $\phi_1 = 0.0$, $\phi_2 = 0.39\pi$, $K_a/2\pi = -0.01 \times 10^6$, $K_b/2\pi = -0.03 \times 10^6$.

- A saddle point occurs when at least one of the $\text{Re}(\lambda_i)$ has a different sign from the others. In this case, the stability will depend on the direction of the eigenvectors related to the eigenvalue sign: when the eigenvalue is positive (negative) the equilibrium in the respective eigenvector direction is unstable (stable).
- For cases where $\text{Re}(\lambda_i) = 0$ the fixed point is said to be non-hyperbolic, and further analysis is required to determine the fixed point stability.

The linear stability analysis for the system parameters in Table I is shown in Fig. 2. Note that there are changes of stability around $|\epsilon|^2 \approx 0.15 \times 10^{10}$, where the fixed points lose their stability in some directions with the attractors becoming saddle points; and $|\epsilon|^2 \approx 1.25 \times 10^{10}$, where the fixed points gain stability in some directions with the saddle points becoming attractors. In our numerical simulations we observe that, for a given set of parameters for our clock system, limit cycles occur when

the $|\epsilon|^2$ is close to the values cited above. Further numerical investigations are required to classify the type of bifurcation the system undergoes. For our purposes, it is sufficient to use the stability analysis as a tool to identify the approximate parameters required to observe limit cycles.

C. Semiclassical dynamical analysis

In order to develop intuition behind the appearance of limit cycles in this system, we consider a simplified model in which all parameters are set equal except the Kerr non-linearities for which $K_a \ll K_b$. We also assume zero detuning and no driving field. As it turns out, limit cycles can arise spontaneously due to noise.

The semiclassical equation of motion for both coherent and measurement-based feedback take the form

$$\dot{\alpha} = -\frac{\kappa}{2}\alpha - g\beta - 2iK_a|\alpha|^2\alpha \quad (23)$$

$$\dot{\beta} = -\frac{\kappa}{2}\beta - g\alpha - 2iK_a|\beta|^2\beta. \quad (24)$$

Furthermore, we define polar coordinates as

$$\alpha = r_a e^{i\theta_a}, \quad \beta = r_b e^{i\theta_b}. \quad (25)$$

Substituting these into the equations of motion we get

$$\dot{r}_a = -\frac{\kappa}{2}r_a - gr_b \cos \phi, \quad (26)$$

$$\dot{r}_b = -\frac{\kappa}{2}r_b - gr_a \cos \phi, \quad (27)$$

$$\dot{\phi} = g \left(\frac{r_b}{r_a} + \frac{r_a}{r_b} \right) \sin \phi - 2(K_a r_a^2 - K_b r_b^2), \quad (28)$$

where $\phi = \theta_a - \theta_b$. Equations of this form have been extensively studied in the context of synchronization of limit cycles [9].

On the synchronised limit cycle, $\dot{\phi} = 0$ and we find that $r_a = r_b = r$ with

$$r^2 = \frac{\sqrt{g^2 - \kappa^2/4}}{|K_b - K_a|} \quad (29)$$

and

$$\sin \phi = \sqrt{1 - \frac{\kappa^2}{4g^2}}. \quad (30)$$

The existence of the limit cycle requires $g > \kappa/2$ and $K_a \neq K_b$. To realise this system experimentally requires careful tailoring of the external and internal coupling rates and is not part of the scope of this work.

To emphasise the advantages of the coherent feedback established here, we compare it to measurement-based feedback in the following section.

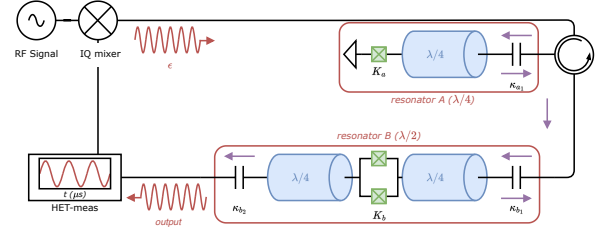


FIG. 3: An equivalent measurement based feedback scheme. The coherent feedback channel is replaced by a heterodyne measurement producing two currents that are used for IQ-modulation of the coherent field driving the $\lambda/4$ resonator.

D. Measurement-based feedback clock

In this section, we derive the equivalent measurement-based feedback model and compare it to the one for coherent feedback. The scheme is shown in shown in Fig. 3. Note that operator hats are omitted for the remainder of this section. The field exiting to the left of cavity B is subject to heterodyne detection. This produces two quadrature stochastic currents $J_x(t), J_y(t)$ that satisfy the stochastic differential equations

$$J_x(t) = \kappa_{b,o} \langle b + b^\dagger \rangle_c + \sqrt{2\kappa_{b,o}} dW_x, \quad (31)$$

$$J_y(t) = -i\kappa_{b,o} \langle b - b^\dagger \rangle_c + \sqrt{2\kappa_{b,o}} dW_y. \quad (32)$$

A complex stochastic process $J_{het}(t) = \frac{1}{2}(J_x(t) + iJ_y(t))$ depends on the conditional quantum mean cavity field as

$$J_{het}(t)dt = \kappa_{b,o} \langle b \rangle_c(t) + dZ(t), \quad (33)$$

where $dZ(t) = \sqrt{\kappa_{b,o}/2}(dW_x(t) + idW_y(t))$ is a complex valued Wiener process. The conditional mean is given by $\langle b \rangle_c(t) = \text{Tr}[\rho_c(t)b]$ and the conditional state obeys the stochastic master equation [4]

$$d\rho_c(t) = -i[H, \rho]dt + \kappa_a \mathcal{D}[a]\rho_c dt + \kappa_b \mathcal{D}[b]dt + \mathcal{H}[dZ^*(t)b]\rho_c. \quad (34)$$

The heterodyne current modulates the field input from the left using a IQ modulator. The feedback Hamiltonian is

$$H_{fb} = \lambda(J_x(t)X + J_y(t)Y), \quad (35)$$

where $X = (ae^{-i\phi} + a^\dagger e^{i\phi})$, $Y = -i(ae^{-i\phi} - a^\dagger e^{i\phi})$ and λ is a dimensionless parameter that accounts for the feedback strength.

If we then average over all stochastic currents, the measurement-based feedback master equation is given

by [3]

$$\begin{aligned} \frac{d\rho}{dt} = & -i[H, \rho] + \kappa_b \mathcal{D}[b]\rho + \kappa_a \mathcal{D}[a]\rho \\ & - i\lambda\sqrt{\kappa_{b_2}\kappa_{a_1}}[X, b\rho + \rho b^\dagger] - i\lambda\sqrt{\kappa_{b_2}\kappa_{a_1}}[Y, -ib\rho + i\rho b^\dagger] \\ & + \lambda^2\kappa_{a_1}\kappa_{b_2}(2\mathcal{D}[Y]\rho + 2\mathcal{D}[X]\rho) \\ & - \sqrt{\kappa_{a_1}\kappa_{b_1}}([b^\dagger, a\rho] + [\rho a^\dagger, b]). \end{aligned} \quad (36)$$

Here, the Hamiltonian is

$$\begin{aligned} H = & \epsilon(a + a^\dagger) + \Delta_a a^\dagger a + \Delta_b b^\dagger b \\ & + K_a a^{\dagger 2} a^2 + K_b b^{\dagger 2} b^2, \end{aligned} \quad (37)$$

where we use the interaction picture. The semiclassical equations of motion are

$$\begin{aligned} \dot{\alpha} = & -\left(i\Delta_a + \frac{\kappa_a}{2}\right)\alpha - 2iK_a|\alpha|^2\alpha - i\epsilon \\ & - 2i\lambda\sqrt{\kappa_{a_1}\kappa_{b_2}}\beta e^{i\phi}, \end{aligned} \quad (38)$$

$$\dot{\beta} = -\left(i\Delta_b + \frac{\kappa_b}{2}\right)\beta - 2iK_b|\beta|^2\beta - \sqrt{\kappa_{a_1}\kappa_{b_1}}\alpha. \quad (39)$$

Apart from the driving term, these are the same as Eqs. (13,14) derived for the coherent feedback, if we choose $\phi = \pi/2$, $\lambda = 1/2$ and neglect losses and relative phases. The resulting dynamics is the same and limit cycles occur for the same parameter values.

III. NOISE ANALYSIS

We can convert the master equation to an equivalent stochastic process in an extended phase-space using the generalized P representation of Drummond and Gardiner [10]. The state of the two-mode system may be written as

$$\rho = \int_D \Lambda(\boldsymbol{\alpha}, \boldsymbol{\beta}) P(\boldsymbol{\alpha}, \boldsymbol{\beta}) d\mu(\boldsymbol{\alpha}, \boldsymbol{\beta}) \quad (40)$$

where $\boldsymbol{\alpha} = (\alpha_a, \alpha_b)$, $\boldsymbol{\beta} = (\beta_a, \beta_b)$. The non-diagonal coherent state projection operator is defined as

$$\Lambda(\boldsymbol{\alpha}, \boldsymbol{\beta}) = \frac{|\boldsymbol{\alpha}\rangle\langle\boldsymbol{\beta}^*|}{\langle\boldsymbol{\beta}^*|\boldsymbol{\alpha}\rangle}, \quad (41)$$

and $d\mu(\boldsymbol{\alpha}, \boldsymbol{\beta})$ is an integration measure defining different representations. The Glauber-Sudarshan P function assumes that the stochastic dynamics never leaves the classical subspace $\boldsymbol{\beta} = \boldsymbol{\alpha}^*$, and this is not the case when a Kerr nonlinearity is included.

A. Coherent feedback

The Fokker-Planck equation is

$$\begin{aligned} \frac{\partial P}{\partial t} = & \sum_{\nu=a,b} \left[\frac{\partial}{\partial\alpha_\nu} (\kappa'_\nu \alpha_\nu + 2iK_\nu \alpha_\nu^2 \beta_\nu) \right. \\ & + \frac{\partial}{\partial\beta_\nu} (\kappa''_\nu \beta_\nu - 2iK_\nu \beta_\nu^2 \alpha_\nu) \\ & - iK_\nu \frac{\partial^2}{\partial\alpha_\nu^2} \alpha_\nu^2 + iK_\nu \frac{\partial^2}{\partial\beta_\nu^2} \beta_\nu^2 \\ & + \bar{\epsilon} \frac{\partial}{\partial\alpha_b} + \bar{\epsilon}^* \frac{\partial}{\partial\beta_b} \\ & \left. + g_b(\alpha_a \frac{\partial}{\partial\alpha_b} + \beta_a \frac{\partial}{\partial\beta_b}) + g_a(\alpha_b \frac{\partial}{\partial\alpha_a} + \beta_b \frac{\partial}{\partial\beta_a}) \right] P, \end{aligned} \quad (42)$$

where $\kappa'_a = -i\Delta_a + \kappa_a/2$ and $\kappa'_b = -i\Delta'_b + \kappa_b/2$. Note that the coherent feedback term does not add any second order derivatives. This indicates that it does not add any additional noise. The noise is determined by the quantum noise arising from the Kerr nonlinearities alone.

B. Measurement-based feedback

The terms in Eq. (36) that contribute classical diffusion noise due to measurement-based feedback are

$$\begin{aligned} \frac{d\rho}{dt} = & \dots + \lambda^2\kappa_{a_1}\kappa_{b_2}(2\mathcal{D}[Y]\rho + 2\mathcal{D}[X]\rho) \\ = & \dots - \lambda^2\kappa_{a_1}\kappa_{b_2}([X, [X, \rho]] + [Y, [Y, \rho]]) \end{aligned} \quad (43)$$

In this form, we see that these terms drive a classical diffusion process in X and Y at the rate $\Gamma = \lambda^2\kappa_{a_1}\kappa_{b_2}$. This is absent from the coherent feedback master equation. Such terms contribute second order derivatives to the Fokker-Planck equation of the form

$$\begin{aligned} \frac{\partial P}{\partial t} = & \dots + \Gamma \left(\frac{\partial}{\partial\alpha_a} + \frac{\partial}{\partial\beta_a} \right)^2 P \\ & + \Gamma \left(\frac{\partial}{\partial\alpha_a} - \frac{\partial}{\partial\beta_a} \right)^2 P \end{aligned} \quad (44)$$

We conclude that the coherent feedback process must necessarily be less noisy than the measurement-based feedback process given otherwise equivalent system parameters.

IV. EXPERIMENTAL REALISATION

A. Nonlinear microwave resonators

To show the feasibility of coherent feedback and its application for a quantum clock, we experimentally realise the feedback circuit using a system of coupled nonlinear superconducting resonators. While the proposed clock

can in principle be implemented in other platforms such as photonic or optomechanical systems, our approach offers multiple advantages including control over certain design parameters, in particular, the coupling rates and the Kerr nonlinearities. The geometric coupling rates are determined by the dimensions of the capacitors connecting the resonators to the transmission lines and can be modelled using a finite-element simulation software. To implement the Kerr nonlinearities, we terminate the $\lambda/4$ -resonator by a single Josephson junction shorted to ground and intersect the $\lambda/2$ -resonator B by a SQUID, which enables us to tune the resonance frequency ω_b in situ and, consequently, the detuning between the resonators. The necessary magnetic flux is supplied by a current-threaded copper coil attached to the bottom of the sample holder. Although this nonlinearity is not strictly necessary for the emergence of limit cycles, it adds an additional degree of freedom to the system to reach the necessary parameter regime. This is especially important since we do not have direct control over the losses and relative phases between the resonators, which affect the range in which limit cycles emerge. Additionally, the simulated model is semiclassical and does not include noise, so deviations from the predicted regime are expected. In the context of a clock, the nonlinearity in the oscillator system is equivalent to having the oscillator of a pendulum clock driven beyond its linear approximation regime.

The required nonlinearities are small compared to the resonator loss rates $K/\kappa \ll 1$, similar to the regime used for JPAs and tunable couplers. This enables us to discard the cross-Kerr and beamsplitter-like interaction terms between different modes and leaves us with the self-Kerr terms in Eq. (4).

Since we need to design our system parameters as accurately as possible in order to reach the regime where limit cycles occur, it is necessary to find explicit expressions for the resonator coupling rates, the Kerr nonlinearities and the resonator frequencies. Following the approach detailed in Ref. [11], we start from the Lagrangian for a coplanar waveguide (CPW) of length d intersected or terminated by a Josephson junction and find the boundary conditions at the open and closed ends of the CPW and at the junctions. Inserting the standard ansatz for travelling modes into the boundary conditions at the junction results in a transcendental equation for the wave numbers. Using that the junction capacitances C_J are much smaller than the capacitance of the coplanar waveguides $C_J/(C_0 d_{a,b}) \ll 1$, where C_0 is the capacitance of the waveguide per unit length and $d_{a,b}$ are the geometric lengths of the resonators, results in the following approximate expressions for the fundamental modes

$$k_a^{(0)} l_a \approx \frac{\pi}{1 + \gamma_a}, \quad k_b^{(0)} l_b \approx \frac{\pi}{2(1 + \gamma_b)}. \quad (45)$$

Here, we define the inductive participation ratio as

$$\gamma_i = \frac{L_{Ji}}{L_0 d_i} \ll 1, \quad (46)$$

where L_{Ji} is the Josephson inductance and L_0 the geometric inductance per unit length of resonators A ($i = a$) and B ($i = b$). This allows us to write analytical expressions for the effective resonator frequencies (dressed by the junction inductances) as

$$\omega_a \approx \frac{\omega_a^{(0)}}{1 + \gamma_a}, \quad \omega_b(F) \approx \frac{\omega_b^{(0)}}{1 + \frac{\gamma_b}{|\cos(F)|}}, \quad (47)$$

where $\omega_i^{(0)}/2\pi = (L_0 C_0)^{-1/2}$, $F = \pi\Phi/\Phi_0$ with Φ the external magnetic flux threading the SQUID loop and Φ_0 is the flux quantum. While both resonator frequencies are reduced by the presence of the junctions, applying an external flux to resonator B allows us to further decrease the frequency. Choosing $\omega_b(0) > \omega_a$ enables us to tune the resonators to the desired detuning and compensate for slight frequency deviations between the designed and the fabricated circuit. The geometric coupling rates are modified by the junctions as well, resulting in the following expressions for the effective coupling rates

$$\kappa_{a_1} \approx \frac{\kappa_{a_1}^{(0)}}{1 + 4\gamma_a}, \quad \kappa_{b_{1,2}}(F) \approx \frac{\kappa_{b_{1,2}}^{(0)}}{1 + 4\frac{\gamma_b}{|\cos(F)|}}, \quad (48)$$

where $\kappa_{i,1,2}^{(0)}$ ($i = a, b$) are the geometric coupling rates of the resonators. These differences between the bare and effective resonator frequencies and coupling rates have to be taken into account when designing the circuit.

We obtain the Hamiltonians for the nonlinear resonators by performing a Legendre transformation and substituting the creation and annihilation operators introduced in Eq. (4). Expanding the nonlinear Josephson junction potential to second order, an approximation valid for small nonlinearities, and changing to the frame of the drive at frequency ω_ϵ , yields

$$\hat{H}_a = \Delta_a \hat{a}^\dagger \hat{a} + K_a \hat{a}^{\dagger 2} \hat{a}^2, \quad (49)$$

$$\hat{H}_b(F) = \Delta_b(F) \hat{b}^\dagger \hat{b} + K_b(F) \hat{b}^{\dagger 2} \hat{b}^2 \quad (50)$$

with the detunings $\Delta_{a,b}$ as defined in Eq. (1) and the flux dependencies explicitly stated. The coefficients of the fourth-order terms in $H_{a,b}$ are the self-Kerr nonlinearities and given by

$$K_a = -\frac{E_{Ja}}{4\hbar} \left(\frac{\varphi_{zpf}}{\varphi_0} \right)^4 \cos\left(\frac{\pi}{2(1 + \gamma_a)} \right), \quad (51)$$

$$K_b(F) = -\frac{E_{Jb}}{2\hbar} \left(\frac{\varphi_{zpf}}{\varphi_0} \right)^4 \cos\left(\frac{\pi}{2\left(1 + \frac{\gamma_b}{|\cos(F)|}\right)} \right), \quad (52)$$

where $\varphi_{zpf} = \sqrt{\hbar/(2\omega_{a,b}^{(0)} C_0 d_{a,b})}$ and $\varphi_0 = \Phi_0/(2\pi)$ are the flux zero-point fluctuation and the reduced flux quantum, respectively, and $E_{Ji} = \varphi_0^2/L_{Ji}$ with $i = (a, b)$.

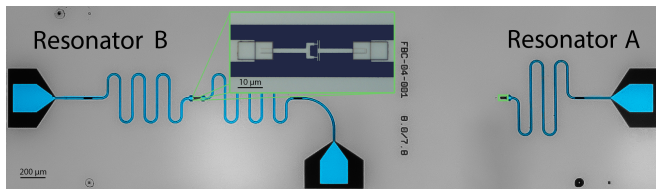


FIG. 4: Optical micrograph of the feedback circuit. The nonlinear resonators A (B) are shorted to ground (intersected) by a single junction (SQUID) with the location indicated by the green rectangle. A close-up of the SQUID, fabricated using double-angle evaporation is shown in the inset. The resonators are capacitively coupled to the the drive and readout circuitry via superconducting transmission lines (see the schematic in Fig. 1).

We solve Eq. (51) and Eq. (52) numerically to find the Josephson energies corresponding to the required Kerr nonlinearities. Having explicit expressions for all variables in Eqs. (13, 14), we are able to choose suitable fabrication parameters for the regime where stable limit cycles appear in the semiclassical simulations.

The device is fabricated using a standard process for superconducting circuits: First, the resonators are patterned in Aluminium on a Silicon substrate using electron-beam lithography and wet etching. Next, the Josephson junctions for the single junction and the SQUID are deposited via double-angle evaporation of aluminium and dynamic oxidation of aluminium oxide. Finally, the device is packaged and mounted in a dilution refrigerator and cooled to a temperature of 70 mK. Details about the measurement setup and the data acquisition are given in Appendix C.

B. Characterisation

We first characterise both CPW resonators in a separate cool down without the feedback loop by applying an attenuated microwave signal directly to the input port of each resonator and measuring the response in reflection. From fitting the signal to an inverse Lorentzian, we extract the internal and external quality factors that give the loss rates $\kappa_{a,b}$ of the feedback clock system. To determine the Kerr nonlinearities $K_{a,b}$, we extract the inductive participation ratios $\gamma_{a,b}$ which are defined in Eq. (46). While $L_0 d_{a,b}$ is determined by the dimensions of the coplanar waveguide resonator which is controlled by the resonator geometry, the Josephson inductances $L_{J,a,b}$ are determined by the junction parameters, i.e. the junction area and the oxide thickness. Due to uncertainties in the fabrication process, these values can deviate from the design.

An initial estimation for $L_{J,a}$ is obtained from measuring the critical current at room temperature using the Ambegaokar-Baratoff relation. At cryogenic tempera-

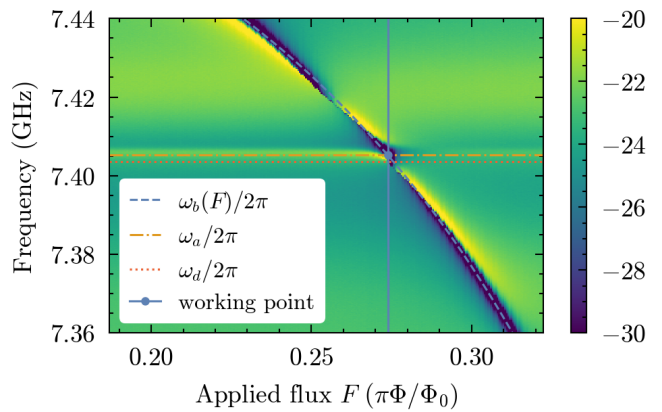


FIG. 5: Partial flux sweep for resonator B. The resonance frequency ω_b decreases as the applied flux, increases according to Eq. (47). The fixed frequency of resonator a ω_a and the set drive frequency ω_ϵ are shown in orange (dash-dotted) and green (dotted), respectively, and the flux working point at $F = 0.274\pi$, used for the limit cycle measurements in this paper, is indicated by the red vertical line.

tures, a more precise way to determine $L_{J,a}$ is to measure the effective frequency ω_a and get γ_a from Eq. (47), using the design values for L_a , l_a and ω_a^0 . For the tunable resonator B, we sweep the external magnetic flux resulting in a π -periodic modulation of the resonance frequency $\omega_b(F)$, as partially shown in Fig. 5. Fitting such a curve to Eq. (47) and using the flux periodicity yields the SQUID inductance $L_{J,b}$. From $\gamma_{a,b}$, we finally calculate K_a and $K_b(F)$ using Eqs. (51) and (52), respectively.

Parameter	Value	Unit
$F = \pi\Phi/\Phi_0$	0.274π	—
$\omega_a/2\pi$	7.4060	GHz
$\omega_b(0)/2\pi$	7.4960	GHz
$\omega_b(F)/2\pi$	7.4053	GHz
$\omega_\epsilon/2\pi$	7.4035	GHz
$\Delta_a/2\pi$	1.80	MHz
$\Delta_b(F)/2\pi$	1.80	MHz
$K_a/2\pi$	-0.01	MHz
$K_b(0)/2\pi$	-0.01	MHz
$K_b(F)/2\pi$	-0.03	MHz
$\kappa_a/2\pi$	3.20	MHz
$\kappa_{a_{\text{int}}}/2\pi$	0.11	MHz
$\kappa_{b1,2}(0)/2\pi$	2.64	MHz
$\kappa_{b1,2}(F)/2\pi$	2.52	MHz
$\kappa_{b_{\text{int}}}/2\pi$	1.64	MHz

TABLE I: System parameters of the superconducting circuit used for the measurements. The values are determined from the characterisation of the resonators. See the main text for details.

After the resonators are characterised, we add the remaining parts of the feedback circuit as shown in Fig. 4. Driving the system through the directional coupler and measuring the signal reflected off resonator B and transmitted via the circulator shows both resonators appear as dips in the transmission amplitude (dashed blue line and dash-dotted orange line in Fig. 5). From this, we identify the flux value where the resonance frequencies coincide. We expect limit cycles to appear near this working point.

The drive power applied to the circuit is determined by the total attenuation in the microwave input line and related to the photon number rate ϵ^2 by $P_{\text{dBm}} = 10 \log_{10}(\hbar\omega\epsilon^2) + 30$, and set to the range where the limit cycles are expected to appear. The relative phase between the resonators, $\varphi_{1,2}$, and the loss coefficients, $\eta_{1,2}$, cannot be measured directly and are kept as free parameters that can be fixed by comparing the simulations to the experimental results.

V. RESULTS

After sweeping the power and frequency of the drive and the frequency of resonator B around resonator A within the range suggested by the semiclassical equations of motion, we observe the emergence of limit cycles for a range of parameters. For the following measurements, we choose settings that allow for a clear observation of the limit cycles through a wide range of driving powers. The system parameters used are shown in Table I.

The signal emitted from the clock system through the bottom circulator in Fig. 1 comprises primarily of the photons reflected from resonator B and needs to be amplified to be registered at room temperature. This is achieved through an amplification chain containing a quantum-limited amplifier, a high-electron mobility transistor at 4 Kelvin and two room-temperature amplifiers. The signal is then processed using a heterodyne detection scheme consisting of analogue IQ-demodulation mixing the signal with a local oscillator shifted by 25 MHz from the drive frequency and subsequent digital filtering and downconversion to DC using an analogue to digital converter. We end up with a time series of the quadrature components of the signal, which we can analyse directly or process further.

To explore the properties of the limit cycles, we move to the frequency domain, which, in contrast to the time domain, allows taking averages to increase the signal-to-noise ratio without suppressing the signal itself. We do this by taking the absolute square of the Fourier transform which gives the energy spectral density (ESD). Here, the limit cycles appear as sidebands centred around the driving frequency at 0 Hz.

For the system parameters in Table I, a drive power sweep averaged from 100 repetitions is depicted in the top of Fig. 6. Bifurcation occurs at around -96 dBm and limit cycles emerge at a frequency of around 1.5 MHz (0.6 μs). Increasing the drive power increases the limit cy-

cle frequency up to around 2.0 MHz (0.5 μs) at -89 dBm, beyond which bifurcation doubling splits the limit cycles in two branches. The bottom of Fig. 6 depicts a cutout of the ESD at -92 dBm and shows several distinct features of the sidebands: the significant asymmetries in amplitude and linewidth between the positive and negative sideband and the second harmonic visible in the negative sideband starting from around -3 MHz. Neither of these features are captured by our semiclassical model, and while the second harmonic is likely due to higher-order nonlinearities becoming relevant, the origin of the asymmetry in the sidebands has not yet been identified.

To show the behaviour of the limit cycles with increasing drive power, we extract the centre frequency and the linewidths of the sidebands by fitting the peaks to a Lorentzian. The change of the frequencies and the linewidths are shown in Fig. 7. As expected, the frequency increases with driving power while, in the low-power regime, the linewidth decreases with power as predicted by [12]. The following increase in the linewidth can be likely attributed to higher-order nonlinearities indirectly manifested by the appearance of second harmonics as discussed above.

A. Application as a quantum clock

A clock directly benefits from the reduced noise generated by coherent feedback compared to a measurement-based feedback approach, as the linewidth of the clock signal in frequency is directly related to the accuracy of the timing signal in the time domain. To generate a timing signal, we continuously measure the heterodyne output current of the feedback circuit which gives a complex signal in the time domain $s(t) = I(t) + iQ(t)$ with the in phase and quadrature currents $I(t)$ and $Q(t)$, respectively. The clock ticks are generated from the amplitude

$$A(t) = \sqrt{|s(t)|^2} \quad (53)$$

by normalising and zero-meaning it and applying the sign function (Fig. 8a).

The differences in time between the peaks yield the clock tick period distribution which is fitted to an inverse Gaussian (Wald) distribution

$$W(T, \alpha, \lambda) = \sqrt{\frac{\lambda}{2\pi}} T^{-3/2} \exp\left[-\frac{\lambda}{2\alpha^2 T}(T - \alpha)^2\right], \quad t \geq 0, \quad (54)$$

where α, λ are positive real parameters (λ is called the spread parameter). From the mean $\bar{T} = \alpha$ and the variance $\overline{\Delta T^2} = \alpha^3/\lambda$, we get the clock accuracy N via

$$N = \frac{\bar{T}^2}{\overline{\Delta T^2}} = \frac{\lambda}{\alpha}. \quad (55)$$

For time traces taken at detunings $\Delta_a = 2.0$ MHz and $\Delta_b = 0.8$ MHz, this results in $N \approx 5.1$, as depicted in

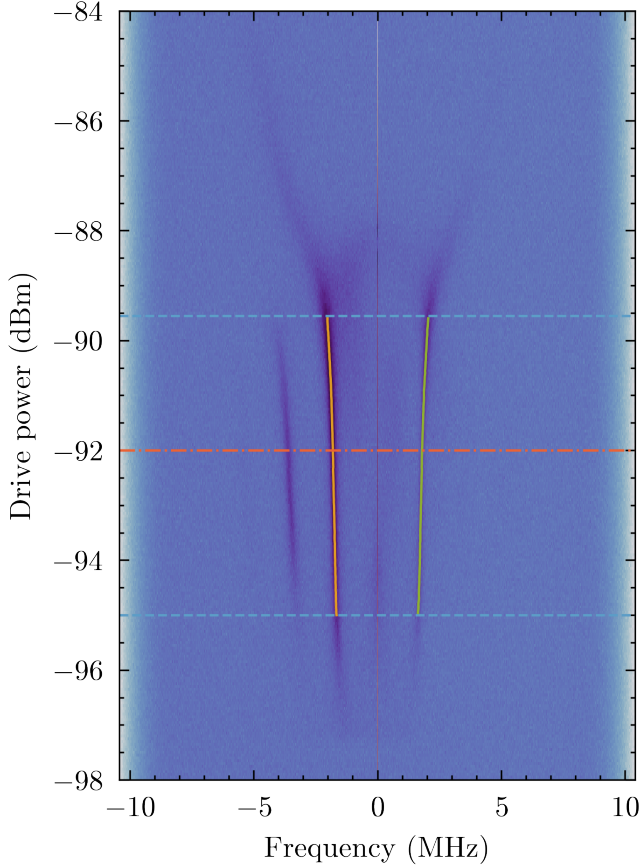


FIG. 6: **(Top)** ESD of a drive power sweep that results in the formation of limit cycles, visible as sidebands from ~ 1.5 MHz. The dashed blue lines indicate the lower and upper boundaries for the drive power used in Fig. 7. The drive signal is visible as a thin line at 0 Hz. **(Bottom)** Cutout of the above sweep at -92 dBm (red dash-dotted line). Visible are the drive in the centre, the sidebands at ~ 2 MHz, asymmetric in amplitude and linewidth, the second harmonic of the negative sideband, and the digital low-pass filter at 10 MHz.

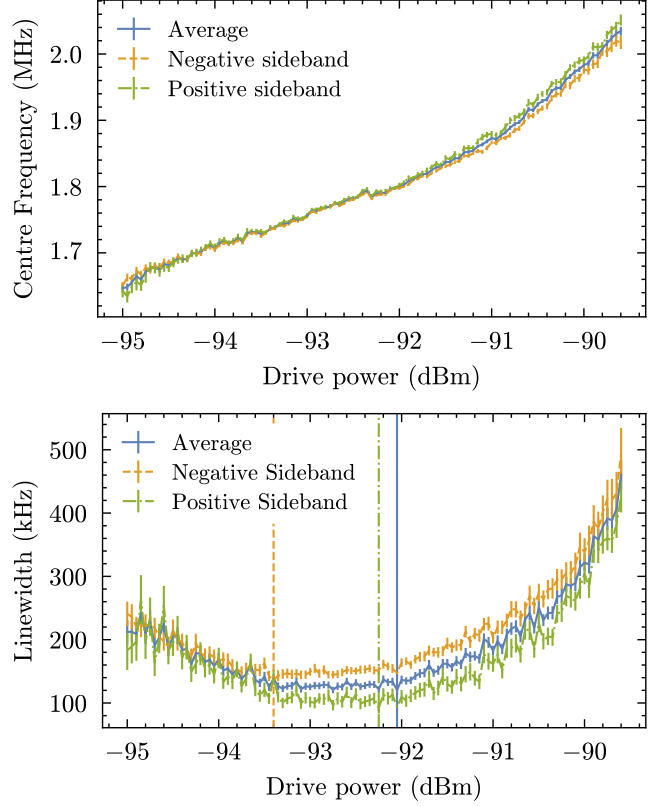


FIG. 7: Sideband frequencies (**top**) and linewidths (**bottom**) in the driving power range indicated in Fig. 6. The centre frequency and linewidths are obtained by fitting to a Lorentzian. The error bars correspond to the standard deviations of the fit parameters.

Fig. 8b. While this is better than a random clock which, by definition, has $N = 2$, it is many orders of magnitude lower than most practical clocks. However, the goal of our experiment is not to surpass existing clocks but to show the implementation of a new feedback scheme which may be used in practical devices to overcome the limitations of the clocks with classical feedback.

Since the linewidths of the sidebands are related to the clock tick distribution by

$$\gamma = \frac{\sigma^2}{\mu^2}, \quad (56)$$

where μ is the amplification rate and σ is the variability of noise (see [13]), they can be used as an additional figure of merit. For our system settings, they reach minima of 136.34 kHz and 92.01 kHz, whereas the average has a minimum of 120.54 kHz, indicated by the vertical lines in the bottom of Fig. 7. A derivation of Eq. (56) is given in Appendix A.

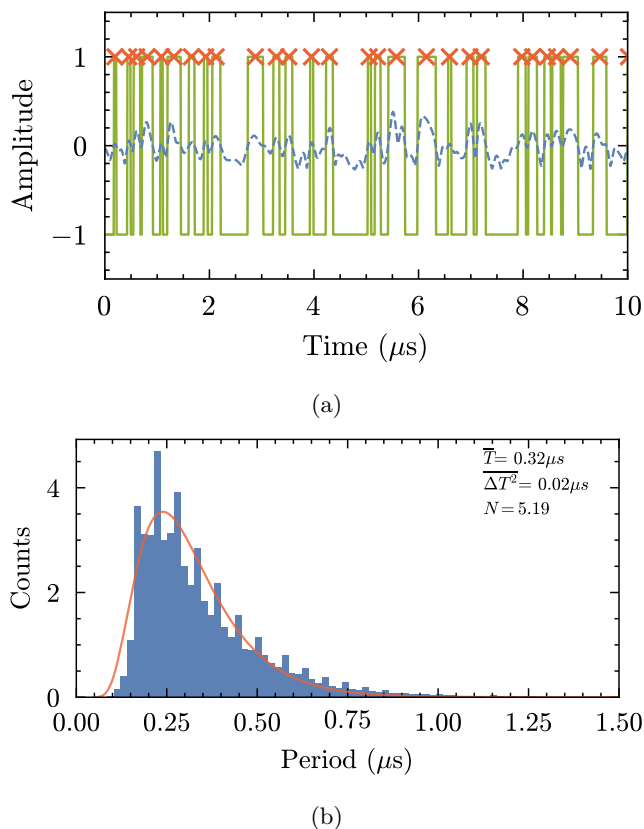


FIG. 8: **(Top)** Cutout of a time series taken for 12.8 ms at -93.5 dBm drive power and with a digital low-pass filter at 4 MHz to remove high-frequency noise (dotted blue line). To extract clock ticks, we zero-centre the data and apply a sign function (green line). The period of the clock ticks is then given by the difference between the peaks (orange crosses). **(Bottom)** Extracted clock ticks fitted to an inverse Gaussian (Wald) distribution with the mean \bar{T} , variance ΔT^2 and corresponding accuracy. The R^2 factor of the fit is 0.93.

B. Towards an autonomous quantum clock

In the previous sections, we drove the system with a coherent drive which can be used as a clock by itself. To understand the effect of the coherence of the drive on the accuracy of our clock, we replace the coherent signal with a noisy driving field. To controllably reduce the coherence of the drive, we modulate the frequency of the drive signal using a white noise signal provided by a function generator with an upper cut-off frequency of 500 kHz. The effect of the frequency noise in the driving field results in the broadening of both the drive signal peak and sidebands in the ESD spectrum.

However, we observe that for a certain drive power range, the linewidth of the positive sideband increases at a lower rate than the linewidth of the drive which leads to a crossover at the frequency modulation amplitude of 0.6 kHz. At stronger modulation the left sideband peak

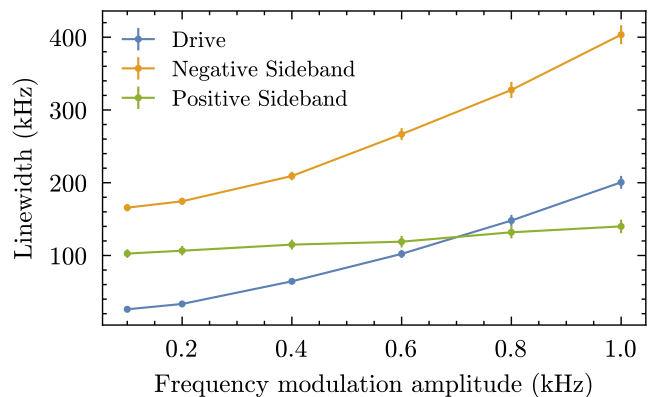


FIG. 9: Linewidths of the noisy drive and sideband as a function of the frequency deviation of the drive signal. Above 0.7 kHz, the linewidth of the drive becomes wider than the left sideband, showing that coherence can be maintained even in the presence of noise. The error bars correspond to the standard deviation of the fit parameter.

becomes narrower than the noisy drive peak, as shown in Fig. 9. This is consistent with the theory in Section II C which suggests that even a fully incoherent drive allows for limit cycles to form in the coherent feedback system.

Although the positive-frequency sideband remains narrow, the negative-frequency sideband broadens approximately at the same rate as the drive signal in the driving power range. To get an advantage in terms of clock performance, it is necessary to create the clock ticks using only the positive sideband signal, disregarding the negative-frequency sideband and the drive.

VI. CONCLUSION

In this paper, we theoretically propose and experimentally realise a new type of quantum clock based on coherent feedback. Unlike traditional clock which rely on measurement-based feedback, our design leverages coherent feedback to suppress noise from quantum measurements, resulting in an improved clock accuracy. Employing semiclassical simulations, the system exhibits stable limit cycles which form the basis for periodic oscillations. We theoretically analyse the quantum noise characteristics of our system and show its inherent superior performance compared to measurement-based feedback. Experimentally, we realise this system using superconducting resonators with embedded Josephson junctions and microwave circulators. Our measurements confirm the emergence of limit cycles and show that the limit cycle oscillations are more coherent than the driving signal under noisy conditions, opening possibilities for implementation of autonomous quantum clocks. The clock's accuracy is characterised in both frequency and time domains, showing promising results for future quantum metrology

applications. While our clock accuracy is not directly comparable with state-of-the-art atomic clocks, we believe that coherent feedback can be used to reach higher accuracy and stability of clock in the future, thus, opening up a new avenue for quantum clock design. In addition to the application as a quantum clock, coherent feedback can be used in a wide range of quantum systems to improve performance and stability beyond the limit of measurement-based feedback.

ACKNOWLEDGMENTS

L.A.M. acknowledges the support from the Brazilian Agency CAPES (Coordenação de Aperfeiçoamento de Pessoal de Nível Superior), Finance Code 88881.128437/2016-01. This project/research was supported by grant number FQXi-IAF19-04 from the Foundational Questions Institute Fund, a donor advised fund of Silicon Valley Community Foundation. We also acknowledge the support of the Australian Research Council Centre of Excellence for Engineered Quantum Systems (EQUS, CE170100009). The authors acknowledge the facilities, and the scientific and technical assistance, of the Australian Microscopy & Microanalysis Research Facility at the Centre for Microscopy and Microanalysis, The University of Queensland. This work used the Queensland node of the NCRIS-enabled Australian National Fabrication Facility (ANFF).

Appendix A: Limit cycles.

The central role of limit cycles in clock design is not widely appreciated. It is a non-trivial mathematical problem to determine the period of the limit cycle using centre manifold theory, done by parametrising the motion on the limit cycle by a phase variable, $\theta(t)$. In the absence of noise we would like this to be fixed by the parameters of the model. The period is then defined as the time take for this variable to move through 2π .

However, noise causes phase diffusion and thus the time taken to move through 2π fluctuates from one cycle to the next. The general theory (phase reduction) [13] shows that the phase noise diffusion rate is slower the larger the limit cycle. For example in the normal form of a limit cycle the equations of motion near a Hopf bifurcation are

$$\dot{x} = [\mu x - \omega y - (x^2 + y^2)y]dt \quad (\text{A1})$$

$$\dot{y} = [\omega x + \mu y - (x + y^2)x]dt + \sigma dW(t), \quad (\text{A2})$$

where μ is the amplification rate. The phase variable on the limit cycle is defined by $x(t) = \sqrt{\mu} \cos(\theta(t))$, $p(t) = \sqrt{\mu} \sin(\theta(t))$. Phase unfolding then gives

$$d\theta(t) = \omega + \frac{\sigma}{\mu} dW(t), \quad (\text{A3})$$

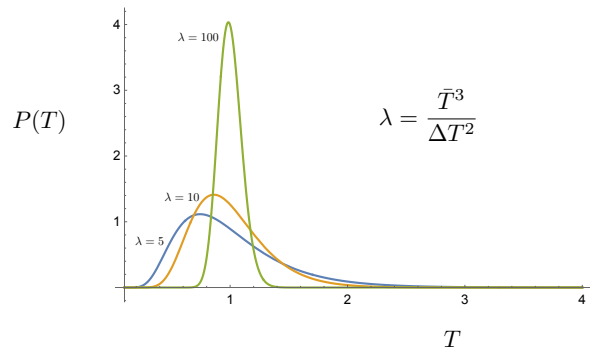


FIG. 10: Mean period $\bar{T} = 1$ and three different values of the spread parameter, λ . Increasing λ is decreasing noise.

i.e., the larger the limit cycle (larger μ) the slower the phase noise. Large limit cycles imply large heat dissipation as the work done in each cycle is dissipated as heat on each cycle, and the more dissipative, the better the clock [12]. A well know example is the laser: the harder it is driven above threshold, the smaller is the phase noise and the smaller the linewidth.

We can find the statistics of the period as a first passage time problem: what is the probability for time T taken for the phase to change by 2π . This is given by the Wald or Inverse Gaussian distribution,

$$W(T, \alpha, \lambda) = \sqrt{\frac{\lambda}{2\pi}} T^{-3/2} \exp \left[-\frac{\lambda}{2\alpha^2 T} (T - \alpha)^2 \right], \quad t \geq 0, \quad (\text{A4})$$

where α, λ are positive real parameters (λ is called the spread parameter). We give an example in Fig. 10. The mean and variance are

$$\bar{T} = \alpha \quad (\text{A5})$$

$$\overline{\Delta T^2} = \frac{\alpha^3}{\lambda}. \quad (\text{A6})$$

The fractional uncertainty is given by

$$\frac{\overline{\Delta T^2}}{\bar{T}^2} = \frac{\alpha}{\lambda}. \quad (\text{A7})$$

For fixed α (fixed mean), this decreases as the spread parameter increases.

In the case of a normal form limit cycle:

$$\bar{T} = \frac{2\pi}{\omega} \quad (\text{A8})$$

$$\overline{\Delta T^2} = \frac{2\pi\sigma^2}{\omega^3\mu}, \quad (\text{A9})$$

fluctuations in period get smaller as the limit cycle gets bigger. If we define the frequency of the clock as

$$f = \frac{1}{T}, \quad (\text{A10})$$

the moments for the frequency are determined by the Wald distribution as

$$\bar{f} = \frac{1}{\alpha} + \frac{1}{\lambda} \quad (\text{A11})$$

$$\overline{\Delta f^2} = \frac{1}{\alpha\lambda} + \frac{2}{\lambda^2}. \quad (\text{A12})$$

The fractional uncertainty in the period is

$$\frac{\overline{\Delta f^2}}{\bar{f}^2} = \frac{\alpha\lambda + 2\alpha^2}{(\alpha + \lambda)^2} \approx \frac{\alpha}{\lambda} \quad (\text{A13})$$

for large λ (low noise). Thus we have the typical result for a good clock

$$\frac{\overline{\Delta T^2}}{T^2} = \frac{\overline{\Delta f^2}}{\bar{f}^2}. \quad (\text{A14})$$

The power spectrum can be calculated directly from the SDE for the phase, Eq. (A3): Define the complex amplitude $z(t)$ such that

$$dz = iz(t)d\theta(t) = iz(t)(\omega dt + \frac{\sigma}{\mu}dW) \quad (\text{A15})$$

. This is the noisy phase oscillator. (See [14] page 104). The stationary two-time correlation function for heterodyne detection is given by

$$\mathbb{E}[z^*(0)z(\tau)] = e^{i\omega\tau - \frac{\sigma^2}{2\mu^2}|\tau|}. \quad (\text{A16})$$

The noise power spectrum is the Fourier transform of this

$$P(\Omega) = \frac{1}{2\pi} \frac{\gamma}{\gamma^2 + (\omega - \Omega)^2}, \quad (\text{A17})$$

where the line width is

$$\gamma = \frac{\sigma^2}{\mu^2}, \quad (\text{A18})$$

a Lorentzian.

Appendix B: Building the SLH triple for the clock

Here, we show how to obtain the Hamiltonian \hat{H} and collapse operators \hat{L}_i for the clock system using the SLH framework [7, 8]. Within this framework, we model each element as a triple of three terms: the scattering matrix \mathbf{S} , the collapse operators \hat{L}_i , and the Hamiltonian \hat{H} , so

$$\mathbf{G}_j = \left(\mathbf{S}, \begin{bmatrix} \hat{L}_1 \\ \hat{L}_2 \\ \vdots \\ \hat{L}_n \end{bmatrix}, \hat{H} \right) \quad (\text{B1})$$

Mathematically, \mathbf{G}_j is the symbol that comprises \mathbf{S} , \hat{L} , and \hat{H} in a single of the j -component in the model.

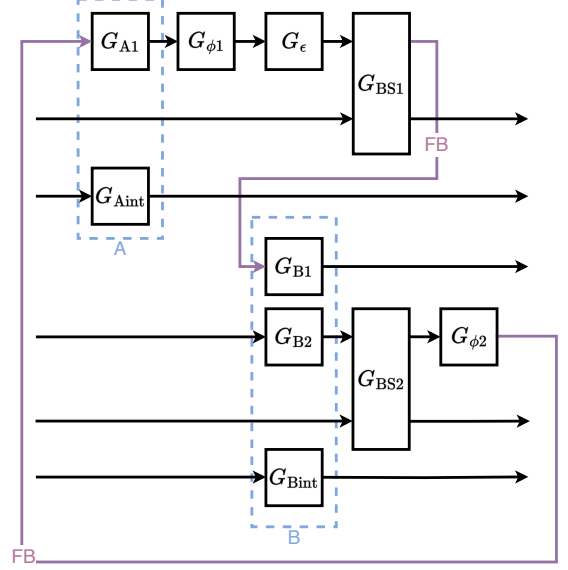


FIG. 11: SLH circuit (with input and output states from left to right) used to derive the equations of motion for the superconducting clock. The internal losses are added as unguided modes while the losses between resonators are modelled by a beamsplitter with reflection coefficient η .

In terms of SLH building blocks, the superconducting clock can be decomposed as shown in Fig. 11. We note that the SLH decomposition is not unique [15] and there are multiple circuits that will describe the same physical system.

First, we write the SLH triple for each of the component used in our decomposition:

The Hamiltonian for each resonator is given by:

$$\hat{H}_i = K_i \hat{i}^\dagger \hat{i}^2 + \Delta_i \hat{i}^\dagger \hat{i}. \quad (\text{B2})$$

with the self-Kerr coefficients $K_i < 0$, the detuning from the drive Δ_i defined in Eq. (1) and $i = a, b$.

1. Coherent Driving Field

$$G_\epsilon = (\mathbb{I}_1, [\epsilon], 0),$$

where \mathbb{I}_1 is the 1×1 identity matrix and ϵ is the amplitude of the driving field.

2. Resonator B - Side 1

$$G_{B1} = (\mathbb{I}_1, [\sqrt{\kappa_{b1}} \hat{b}], H_b).$$

Although we the resonators can be modelled as single elements in the SLH framework, we decompose them into their constituents for our circuit model.

3. Resonator B - Side 2

$$G_{B2} = (\mathbb{I}_1, [\sqrt{\kappa_{b2}} \hat{b}], 0)$$

4. Resonator A - Side 1

$$G_{A1} = (\mathbb{I}_1, [\sqrt{\kappa_{a1}}\hat{a}], H_a).$$

The other side of resonator A is shorted to ground and not explicitly modelled.

5. Resonators internal losses

$$G_{Aint} = (\mathbb{I}_1, [\sqrt{\kappa_{aint}}\hat{a}], 0),$$

$$G_{Bint} = (\mathbb{I}_1, [\sqrt{\kappa_{bint}}\hat{b}], 0)$$

6. Beam Splitters

$$G_{BSi} = \left(\mathbf{S}_{BSi}, \begin{bmatrix} 0 \\ 0 \end{bmatrix}, 0 \right),$$

where $i = 1, 2$ and

$$\mathbf{S}_{BSi} = \begin{bmatrix} \sqrt{1-\eta_i} & \eta_i \\ -\eta_i & \sqrt{1-\eta_i} \end{bmatrix}$$

We use two beam splitters to model losses due to the circulators between cavities A and B.

7. Phase shifter

$$G_{\phi i} = ([e^{(\phi_i)}], [0], 0),$$

We used the phase shifter to model the phases acquired by the travelling field between resonators A and B and B and A.

8. Padding

$$G_{pad} = (\mathbb{I}_1, [0], 0),$$

Padding triplets are used to keep the dimensions of the concatenated elements consistent. Since they do not add any structure to the circuit, they are omitted in Fig. 11.

Following the decomposition shown in Fig. 11, we write the following composition to describe our clock system:

$$\begin{aligned} & \text{FB}\{\text{FB}\{[(G_{BS1} \boxplus G_{pad}) \\ & \triangleleft (G_{\epsilon} \boxplus G_{pad} \boxplus G_{pad}) \\ & \triangleleft (G_{\phi 1} \boxplus G_{pad} \boxplus G_{pad}) \\ & \triangleleft (G_{A1} \boxplus G_{pad} \boxplus G_{Aint}) \\ & \boxplus [(G_{pad} \boxplus G_{BS2} \boxplus G_{pad}) \\ & \triangleleft (G_{pad} \boxplus G_{\phi 2} \boxplus G_{pad} \boxplus G_{pad}) \\ & \triangleleft (G_{B1} \boxplus G_{B2} \boxplus G_{pad} \boxplus G_{Bint})], 0, 3\}, 3, 0\} \end{aligned} \quad (\text{B3})$$

where the feedback (FB), series (\triangleleft) and concatenation (\boxplus) operations for SLH triples are defined as in Refs. [7, 8]. This is the decomposition used to construct the Hamiltonian (equation (4)) and collapse operators (equations (6)) for the superconducting clock system.

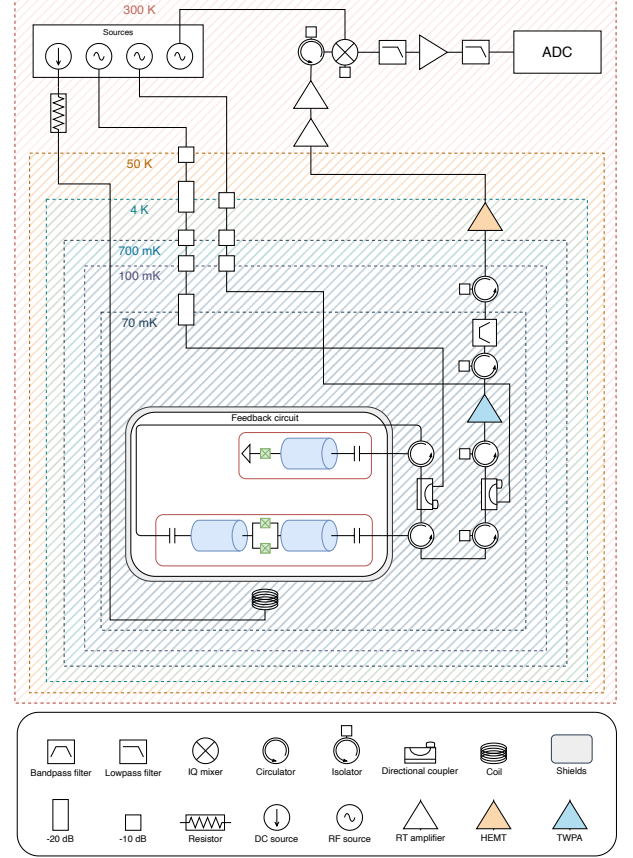


FIG. 12: Wiring diagram for the measurement of the coherent feedback circuit.

Appendix C: Data acquisition

A wiring diagram of the measurement setup is shown in Fig. 12. In the output line, we isolate and amplify the signal using isolators and a TWPA, followed by another isolator, a bandpass filter of 4-8 GHz, another isolator, a HEMT amplifier at 4 K and additional room-temperature amplifiers. The signal is then down-converted to 25 MHz using a Marki IQ mixer and isolated and amplified with a low-pass filter and a room-temperature amplifier. Finally, we digitise the signal using an M4i digitiser card, demodulate the quadratures via digital downconversion to DC and filter high frequencies by a digital FIR filter. We take 4800 samples at a rate of 125×10^6 . For the energy spectral density measurements, we compute the absolute square of the FFT of the complex IQ data and average for 100 repetitions.

-
- [1] J. Levine, *Review of Scientific Instruments* **70**, 2567 (1999).
- [2] G. J. Milburn, *Contemporary Physics* **61**, 69 (2020).
- [3] H. M. Wiseman and G. J. Milburn, *Phys. Rev. A* **49**, 4110 (1994), publisher: American Physical Society.
- [4] H. Wiseman and G. Milburn, *Quantum Measurement and Control* (Cambridge University Press, 2009).
- [5] M. J. Kewming, A. Kiely, S. Campbell, and G. T. Landi, First passage times for continuous quantum measurement currents (2023), arXiv:2308.07810 [quant-ph].
- [6] C. Gardiner and P. Zoller, *Quantum Noise: A Handbook of Markovian and Non-Markovian Quantum Stochastic Methods with Applications to Quantum Optics*, 3rd ed., Springer Series in Synergetics (Springer-Verlag, Berlin Heidelberg, 2004).
- [7] J. Gough and M. James, *IEEE Transactions on Automatic Control* **54**, 2530 (2009).
- [8] J. Gough and M. R. James, *Communications in Mathematical Physics* **287**, 1109 (2009).
- [9] D. G. Aronson, G. B. Ermentrout, and N. Kopell, *Physica D: Nonlinear Phenomena* **41**, 403 (1990).
- [10] D. F. Walls and G. J. Milburn, *Quantum Optics* (Springer, 2008).
- [11] J. Bourassa, F. Beaudoin, J. M. Gambetta, and A. Blais, *Physical Review A* **86**, 013814 (2012), arXiv: 1204.2237.
- [12] P. Erker, M. T. Mitchison, R. Silva, M. P. Woods, N. Brunner, and M. Huber, *Physical Review X* **7**, 10.1103/PhysRevX.7.031022 (2017).
- [13] Z. Aminzare, P. Holmes, and V. Srivastava, in *2019 IEEE 58th Conference on Decision and Control (CDC)* (2019) pp. 4717–4722.
- [14] C. W. Gardiner, *Handbook of Stochastic Processes for Physics, Chemistry and the Natural Sciences* (Springer, 1983).
- [15] J. Combes, J. Kerckhoff, and M. Sarovar, *Advances in Physics: X* **2**, 784 (2017).